Dissipation Losses in Artificial Dielectric Layers

Cavallo, Daniele

DOI
10.1109/TAP.2018.2869241

Publication date
2018

Document Version
Accepted author manuscript

Published in
IEEE Transactions on Antennas and Propagation

Communication

Dissipation Losses in Artificial Dielectric Layers

Daniele Cavallo

***Abstract*— Closed-form expressions to describe artificial dielectric layers (ADLs) with finite conductivity are presented. The propagation of a generic plane wave within the artificial material is described by means of transmission line models, where each layer is represented as an equivalent shunt impedance. The given analytical formulas for the shunt impedance are derived assuming finite conductivity of the metal, thus also an accurate estimation of the losses within the artificial dielectric is obtained from the equivalent circuit. The expressions account for the reactive coupling between the layers due to higher order Floquet modes, thus remain valid even for extremely small electrical distance between layers.**

***Index Terms*—Artificial dielectric layers, closed-form solutions, equivalent circuit.**

I. Introduction

Several of today's radar and wireless communication applications are shifting their operation to higher frequency to fulfill more demanding requirements on resolution, compactness and data rates. When the operating frequency of these systems increases, reaching the millimeter and sub-millimeter waves, the separation of antenna and electronic circuits is no longer possible. Thus, the recent trend is to place the antennas as close as possible to the electronic components, to facilitate the interconnection and to realize highly integrated front-ends. Despite this need, integrated antennas have never showed good performance because of their intrinsic low efficiency: they are limited by problems such as high surface-wave loss, narrow bandwidth, low front-to-back radiation ratio [1]–[3].

Recently, an approach to greatly improve the efficiency of integrated antennas was proposed in [4]: it entails adding artificial dielectric layers (ADLs) above the antennas in order to increase the front-to-back ratio. The artificial dielectric consists of a dielectric slab hosting multiple layers of periodic metal patches, as shown in Fig. 1, where both the patch size and the period are sub-wavelength. This structure is equivalent to an anisotropic slab with an effective refractive index which is higher than that of the dielectric hosting the patches. ADLs realize high effective refractive indexes for propagation normal to stratification and low refractive indexes for grazing incidence. This anisotropic behavior can be exploited to enhance the front-to-back ratio of a near source without exciting surface waves, thus resulting in very high radiation efficiency.

Manuscript received Month DD, YYYY; revised Month DD, YYYY; accepted Month DD, YYYY. Date of publication Month DD, YYYY; date of current version Month DD, YYYY. This work was supported by the Netherlands Organization for Scientific Research (NWO) VENI Grant no. 13673. *(Corresponding author: Daniele Cavallo)*

The author is with the Microelectronics Department, Delft University of Technology, 2628 CD Delft, The Netherlands (e-mail: d.cavallo@tudelft.nl).

Color versions of one or more of the figures in this communication are available online at http://ieeexplore.ieee.org.

Digital Object Identifier XX.XXXX/TAP.XXXX.XXXXXXX

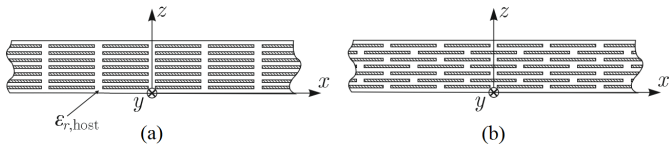

Fig. 1. Two-dimensional side view of artificial dielectric slabs with (a) aligned and (b) shifted layers.

Regarding the analysis, efficient numerical solutions for generic multilayer metasurfaces have been proposed in the past, for example in [5]–[7], and can be used for modeling ADLs. A simplified closed-form analysis of ADLs was presented in [8], [9], valid for aligned layers (Fig. 1(a)), and subsequently generalized in [10] to include the shift between even and odd layers (Fig. 1(b)). Although Fig. 1(b) depicts the case of maximum shift (layers are shifted by half of the period), the shift can be an arbitrary percentage of the unit cell size, realizing an example of glide symmetric structure [11]. It was shown in [10] that the shift greatly increases the effective refractive index of the ADLs with respect to the aligned case, thus it constitutes a key parameter for more flexible designs.

The mentioned previous works [8]–[10] considered only patches made of perfect electric conductor. Losses in ADLs are typically very small because of the sub-wavelength dimensions of the patches, that yield very low current intensity on each patch. However, these losses can vary depending on the illumination, e.g. by a near source or under plane-wave incidence, and they also depend on the polarization and direction of the incident field [12], [13]. For these reasons, it is useful to derive more general analytical formulas that include the finite conductivity of the metal, to accurately quantify the losses and give more physical insight on the nature of Ohmic dissipation in ADLs. In this work, the losses introduced by the finite conductivity of the metal patches in ADLs are analytically characterized and used to derive an effective dissipation factor ($\tan\delta$) for these structures.

II. Single Layer with Finite Conductivity

To clarify the steps of the derivation, it is useful to first consider the problem of a single layer of sub-wavelength lossy patches. This solution will be subsequently generalized to the periodic cascade of layers.

A. Equivalence Theorem and Integral Equation

The initial problem under consideration is a layer of periodic square patches in the x-y plane, infinitely thin in z and illuminated by a generic plane wave with electric and magnetic fields $\mathbf{e}_i$ and $\mathbf{h}_i$. The unit cell of the patch array is shown in

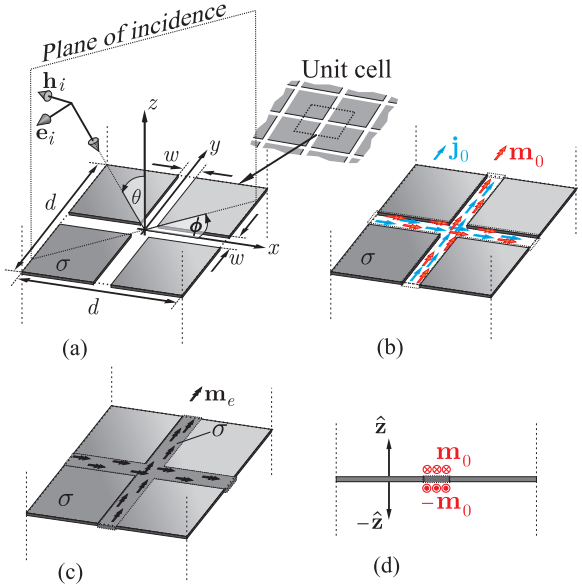

Fig. 2. Unit cell of a single layer of periodic square patches illuminated by a plane wave: (a) Original problem with plane wave incidence; (b) Equivalent problem with magnetic and electric surface currents on the gaps; (c) Equivalent effective magnetic current when the gap is filled with the same metal as the patches; (d) Final equivalent problem with only magnetic currents $\mathbf{m}_0$ with opposite signs above and below.

Fig. 2(a) and it is characterized by period d along both x and y and width of the slots w. Due to the finite conductivity σ, the metal can be described by the surface impedance

$$Z_s = (1+j)\sqrt{\frac{k_0\zeta_0}{2\sigma}} \tag{1}$$

where k_0 and ζ_0 are the free-space wavenumber and impedance, respectively.

The metal surface is modeled using the Leontovich boundary conditions: $\mathbf{e}\times\hat{\mathbf{n}} = Z_s\hat{\mathbf{n}}\times[\mathbf{h}\times\hat{\mathbf{n}}]$, where $\hat{\mathbf{n}}$ is the outward normal unit vector of the surface, and the fields $\mathbf{e}$ and $\mathbf{h}$ denote the total fields, equal to the sum of incident and scattered. By applying the equivalence theorem, the gaps between patches are enclosed with an infinitely thin closed surfaces, on which equivalent electric and magnetic surface current densities $\mathbf{j}_0$ and $\mathbf{m}_0$ are distributed, both above and below (see Fig. 2(b)). The equivalent currents are related to the fields by $\mathbf{j}_0 = \hat{\mathbf{n}}\times\mathbf{h}$ and $\mathbf{m}_0 = \mathbf{e}\times\hat{\mathbf{n}}$.

Proceeding as in [14], the volume enclosed by the surface can be filled with a material having the same conductivity as the metal patches, to obtain a homogeneous layer that is convenient to represent using spectral Green's functions of stratified media. An effective magnetic current density $\mathbf{m}_e$, that account for both $\mathbf{j}_0$ and $\mathbf{m}_0$, can be defined as

$$\mathbf{m}_e = \mathbf{m}_0 + \mathbf{m}_\mathbf{j} = \mathbf{m}_0 + Z_s\hat{\mathbf{n}}\times\mathbf{j}_0 \tag{2}$$

as shown in Fig. 2(c). The continuity of both electric and magnetic fields in the gap implies that the currents above and below the layer are equal and with opposite signs for $\mathbf{m}_0$, but with same sign for $\mathbf{m}_\mathbf{j}$:

$$\mathbf{m}_0^+ = \mathbf{e}^+\times\hat{\mathbf{z}} = \mathbf{e}^-\times(-\hat{\mathbf{z}}) = -\mathbf{m}_0^+ \tag{3}$$

$$\mathbf{m}_\mathbf{j}^+ = Z_s\,\hat{\mathbf{z}}\times(\hat{\mathbf{z}}\times\mathbf{h}^+) = Z_s(-\hat{\mathbf{z}})\times(-\hat{\mathbf{z}}\times\mathbf{h}^-) = \mathbf{m}_\mathbf{j}^- \tag{4}$$

where the superscripts '+' and '−' are used to indicate the current or the field above and below the layer plane. Thus, by imposing the continuity of the tangential magnetic field in the gaps, the following integral equation can be defined:

$$\int_{-\infty}^{\infty}\int_{-\infty}^{\infty} 2\mathbf{m}_0(\boldsymbol{\rho}')\mathbf{g}_{Z_s}(\boldsymbol{\rho}-\boldsymbol{\rho}')d\boldsymbol{\rho}' = -(1+\Gamma)\mathbf{h}_\mathrm{i} \tag{5}$$

where Γ is the reflection coefficient of the magnetic field at the metal, $\boldsymbol{\rho} = x\hat{\mathbf{x}}+y\hat{\mathbf{y}}$ and $\boldsymbol{\rho}' = x'\hat{\mathbf{x}}+y'\hat{\mathbf{y}}$ are the observation and source points respectively, and $\mathbf{g}_{Z_s}$ is the Green's dyadic for magnetic field due to a magnetic source located on the infinite lossy plane. One can note that the magnetic current $\mathbf{m}_\mathbf{j}$ does not contribute to the magnetic field integral equation, since the difference between the field scattered above and below by $\mathbf{m}_\mathbf{j}$ vanishes. Therefore, the integral equation can be written only in terms of magnetic current density $\mathbf{m}_0$ (Fig. 2(d)). This is because, unlike [14], here the Green's functions for the currents above and below the layer are the same.

Equation (5) is solved by expanding of the magnetic current in four domain basis functions, defined on the entire unit cell

$$\mathbf{m}_0(\boldsymbol{\rho}) = \sum_{n=1}^{4} v_n\mathbf{b}_n(\boldsymbol{\rho}) \tag{6}$$

where v_n are unknown coefficients, and the basis functions are defined as in [10]: the functions $\mathbf{b}_1$ and $\mathbf{b}_2$ consist of linear phase terms longitudinally along the x- and y-oriented slots, respectively, to account for the oblique incidence of the plane wave; $\mathbf{b}_3$ and $\mathbf{b}_4$ represent anti-symmetric functions, defined in [8](Eq. (13)), describing the magnetic current distribution at the junction between orthogonal slots. The transverse distribution on the slots is assumed to be constant for all basis functions.

By substituting (6) in (5) and by applying Galerkin projection, we can define a system of equations in matrix form $\overline{\overline{\mathbf{Y}}}\,\overline{\mathbf{v}} = \overline{\mathbf{i}}$, where $\overline{\mathbf{v}} = (v_1, v_2, v_3, v_4)^\mathrm{T}$ is the vector of unknown coefficients, $\overline{\mathbf{i}} = (i_1, i_2, i_3, i_4)^\mathrm{T}$ is the vector of forcing terms obtained projecting the right hand side of (5) onto the testing functions, and $\overline{\overline{\mathbf{Y}}}$ is a 4×4 matrix whose elements Y_{mn} represent the projection of the field scattered by the n-th basis function onto the m-th testing function. It is convenient to calculate the mutual admittances in the spectral domain as

$$Y_{mn} = -\frac{1}{d^2}\sum_{m_x=-\infty}^{\infty}\sum_{m_y=-\infty}^{\infty}\mathbf{B}_m^*(-k_{xm},-k_{ym})\cdot \mathbf{G}_{Z_s}(k_{xm},k_{ym})\mathbf{B}_n(k_{xm},k_{ym}) \tag{7}$$

where m_x and m_y are the indexes of the Floquet modes, $k_{xm} = k_{x0} - 2\pi m_x/d$ and $k_{ym} = k_{y0} - 2\pi m_y/d$ are the Floquet wavenumbers, which determine $k_{zm} = (k_0^2 - k_{xm}^2 - k_{ym}^2)^{1/2}$; $k_{x0} = k_0\sin\theta\cos\phi$ and $k_{y0} = k_0\sin\theta\sin\phi$ are the propagation constants of the incident plane wave along x and y, respectively, and θ and ϕ are related to the direction of incidence as shown in Fig. 2(a).

In (7), the Fourier transforms of the basis functions $\mathbf{B}_n$ are known in closed form, while the spectral Green's function has to be derived, by solving for the currents i_TE and i_TM

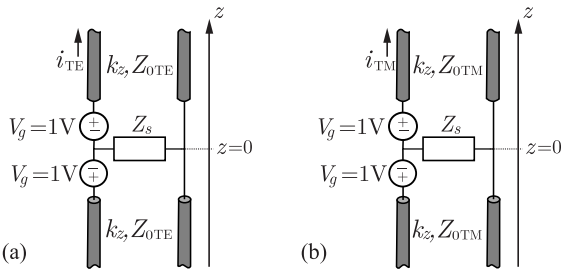

Fig. 3. Equivalent z-transmission lines for the spectral Green's function of the problem: (a) TE and (b) TM modes.

on transmission lines shown in Fig. 3, for transverse electric (TE) and transverse magnetic (TM) modes. The elementary magnetic current sources are represented by unit voltage generators above and below the surface impedance layer. The characteristic impedance of the transmission lines are $Z_{0\text{TE}} = \zeta_0 k_0/k_z$ and $Z_{0\text{TM}} = \zeta_0 k_z/k_0$, where k_z is $(k_0^2 - k_x^2 - k_y^2)^{1/2}$ and the variables k_x and k_y indicate the spectral counterparts of the spatial variables x and y.

The spectral Green's dyadic can be defined as

$$\mathbf{G}_{Z_s}(k_x, k_y) = \begin{pmatrix} -\frac{i_{\text{TE}} k_x^2 + i_{\text{TM}} k_y^2}{k_x^2 + k_y^2} & \frac{(i_{\text{TM}} - i_{\text{TE}}) k_x k_y}{k_x^2 + k_y^2} \\ \frac{(i_{\text{TM}} - i_{\text{TE}}) k_x k_y}{k_x^2 + k_y^2} & -\frac{i_{\text{TE}} k_x^2 + i_{\text{TM}} k_y^2}{k_x^2 + k_y^2} \end{pmatrix} \tag{8}$$

where i_{TE} and i_{TM} are the solution for the currents in the transmission lines in Fig. 3. Solving for the current at $z = 0$ by applyng the Kirchhoff's laws for voltages and currents, leads to

$$i_{\text{TE}}(z{=}0) = \frac{2}{Z_{0TE} + 2Z_s}, \quad i_{\text{TM}}(z{=}0) = \frac{2}{Z_{0TM} + 2Z_s}. \tag{9}$$

B. Equivalent Layer Impedance

Once the Green's function for the lossy metal is obtained, the rest of the steps are very similar to the lossless case [8]. The procedure entails simplifying the admittance matrix $\overline{\overline{\mathbf{Y}}}$ with a few algebraic steps and reducing it to a 2×2 matrix. By projecting the system of two equations on the TE and TM components, the closed-form expressions of the admittance matrix terms leads to the following expression for the equivalent layer impedance:

$$Z_{\text{layer,TE}} = \frac{1}{Y_{\text{TE}}} + Z_s, \qquad Z_{\text{layer,TM}} = \frac{1}{Y_{\text{TM}}} + Z_s \tag{10}$$

where Y_{TE} and Y_{TM} are no longer pure susceptances as in the lossless case, but they are given by

$$Y_{\text{TE}} \approx 2 \sum_{m_y \neq 0} |\text{sinc}(k_{ym} w/2)|^2 \cdot \left(\frac{k_{x0}^2}{2k_{ym}^2} \left(\frac{\zeta_0 k_0}{k_{zm}} + 2Z_s \right)^{-1} + \left(\frac{\zeta_0 k_{zm}}{k_0} + 2Z_s \right)^{-1} \right) \tag{11}$$

$$Y_{\text{TM}} \approx 2 \sum_{m_x \neq 0} |\text{sinc}(k_{xm} w/2)|^2 \cdot \left(\frac{k_{y0}^2}{k_{xm}^2} \left(\frac{\zeta_0 k_0}{k_{zm}} + 2Z_s \right)^{-1} + \left(\frac{\zeta_0 k_{zm}}{k_0} + 2Z_s \right)^{-1} \right). \tag{12}$$

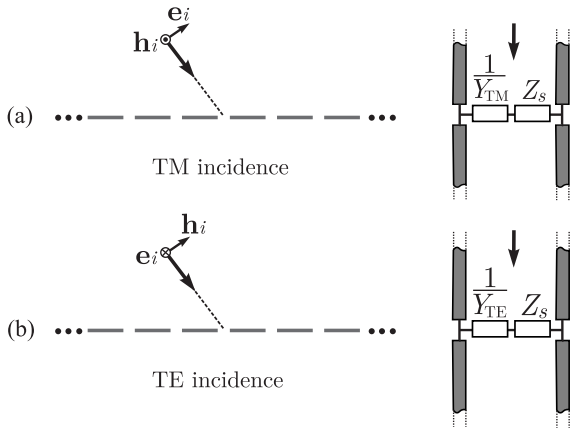

Fig. 4. Equivalent circuit representation of the single layer of patches with finite conductivity for (a) TM and (b) TE incidence.

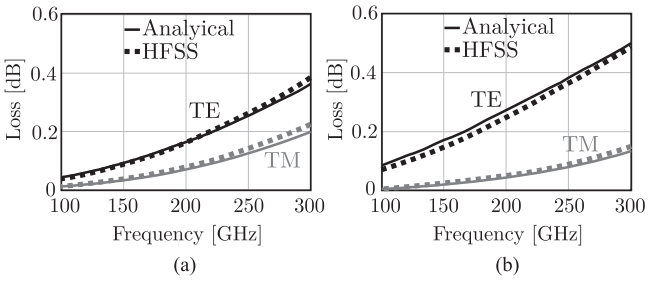

Fig. 5. Comparison of losses calculated with the analytical solution and HFSS simulation, for a single layer of patches with conductivity $\sigma = 1000$ S/m and two angles of incidence: (a) $\theta = 40°$, $\phi = 0°$; (b) $\theta = 60°$, $\phi = 0°$. The geometrical parameters are $d = 0.095\lambda_0$ and $w = 0.01\lambda_0$, with λ_0 being the wavelength at 300 GHz.

Equations (10), (11) and (12) are also valid for the lossless case, by simply imposing $Z_s = 0$. Figure 4 shows the circuit representation of the equivalent layer impedance. The finite conductivity introduces an impedance term Z_s that is in series with the layer impedance. However, the term Z_s is not the only contribution to the resistance, as also the impedances $1/Y_{\text{TE}}$ and $1/Y_{\text{TM}}$ have a comparable resistive component.

To quantify the effect of the finite conductivity, the losses are defined as $\text{Loss(dB)} = -10\log_{10}(|S_{11}|^2 + |S_{12}|^2)$, where S_{11} and S_{12} are the reflection and transmission coefficients of the incident plane wave, respectively. To validate the derived expressions, Fig. 5 compares the losses obtained with the analytical solutions and HFSS simulations. Since the losses of the structure with realistic conductivity values are negligible, an unrealistically low conductivity of $\sigma = 1000$ S/m is taken for the validation. The geometrical parameters are $d = 0.095\lambda_0$ and $w = 0.01\lambda_0$, with λ_0 being the wavelength at 300 GHz. The incident plane wave is impinging at oblique angles ($\theta = 40°, \phi = 0°$ and $\theta = 60°, \phi = 0°$). The comparison between the analytical circuit model and HFSS simulations shows good agreement for all the considered examples.

It can be noted from Fig. 5 that the loss calculated for TE incidence is generally larger than the value observed for TM incidence. This phenomenon likely happens due to the occurrence of electric current loops that are supported by the patches under TE incidence. Figure 6(a) shows the electric

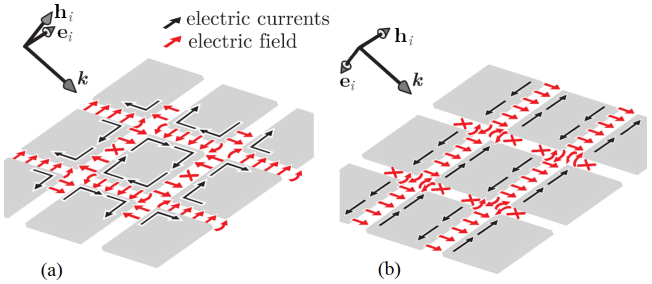

Fig. 6. Illustration of the electric field and electric current distribution on a single layer of periodic patches for (a) TE and (b) TM incidence. The electric field propagating in the slots is consistent with electric current loops in the patches only in the TE case.

field distribution on the single layer for TE incidence, and the correspondent electric currents on the patches forming loops. On the contrary, the TM incidence does not support such current loops, but only excites singly polarized currents on the patches, as shown in Fig. 6(b). The current loops are associated with a longer electrical length (closer to the resonance), which yields higher current intensity and thus increased Ohmic losses.

III. Multiple Layer with Finite Conductivity

Following the same procedure used in [9], [10], the analysis can be expanded to account for a finite cascade of layers. This allows to quantify analytically the losses in ADLs already in the early phase of the design process. The steps are omitted, as they are similar to the ones described in the previous publications. However, they lead to different expressions that include the finite conductivity of the metal.

We consider a plane wave incident on a finite cascade of layers at distance d_z, with arbitrary shift between even and odd layers (indicated by s, equal along x and y), as shown in Fig. 7(a). The equivalent circuit representation in Fig. 7(b) can be used, where the admittances of the layers are separated into infinite-cascade and semi-infinite-cascade solutions, to describe the middle layers and the layers at the edges, respectively. To account for the reactive coupling between layers, the admittances terms in (11) and (12) are now generalized as follows:

$$Y_{\infty\mathrm{TE}} \approx 2 \sum_{m_y \neq 0} |\mathrm{sinc}(k_{ym} w/2)|^2 S_\infty \cdot \left(\frac{k_{x0}^2}{2k_{ym}^2} \left(\frac{\zeta_0 k_0}{k_{zm}} + 2Z_s S_\infty \right)^{-1} + \left(\frac{\zeta_0 k_{zm}}{k_0} + 2Z_s S_\infty \right)^{-1} \right) \quad (13)$$

$$Y_{\infty\mathrm{TM}} \approx 2 \sum_{m_x \neq 0} |\mathrm{sinc}(k_{xm} w/2)|^2 S_\infty \cdot \left(\frac{k_{y0}^2}{k_{xm}^2} \left(\frac{\zeta_0 k_0}{k_{zm}} + 2Z_s S_\infty \right)^{-1} + \left(\frac{\zeta_0 k_{zm}}{k_0} + 2Z_s S_\infty \right)^{-1} \right) \quad (14)$$

where we introduced the term S_∞ given by

$$S_\infty = -j \cot\left(\tfrac{-j2\pi|m|d_z}{d}\right) + j e^{j2\pi m \frac{s}{d}} \csc\left(\tfrac{-j2\pi|m|d_z}{d}\right) \quad (15)$$

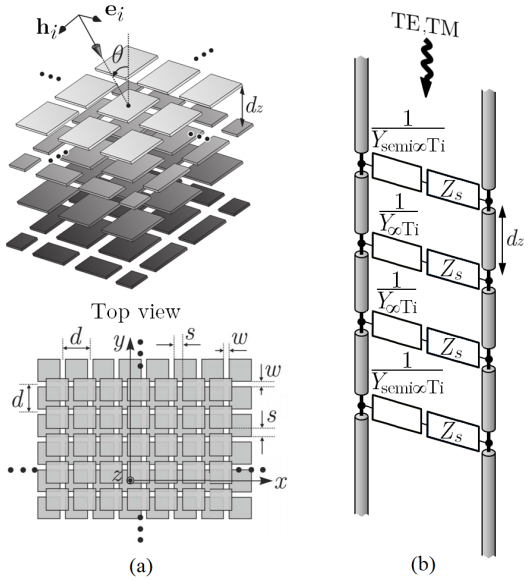

Fig. 7. Plane wave incident on a ADL with finite number of layers: (a) geometry of the problem and (b) equivalent circuit representation for TE and TM components. The subscript 'Ti' can refer to either TE or TM.

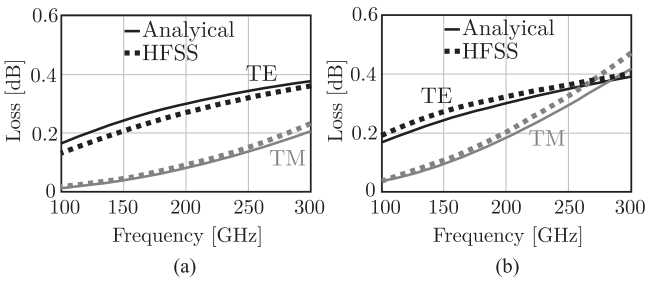

Fig. 8. Comparison of losses calculated with the analytical solution and HFSS simulation, for a three-layer ADL with conductivity $\sigma = 1000$ S/m and angle of incidence $\theta = 60°$, $\phi = 0°$. The geometrical parameters are $d = 0.095\lambda_0$, $w = 0.01\lambda_0$, $d_z = 0.02\lambda_0$, with λ_0 being the wavelength at 300 GHz, and shift (a) $s = 0$ (aligned) and (b) $s = d/2$.

with the index m indicating either m_x or m_y. The admittances for the edge layers (first and last layers) have the same expressions, but replacing S_∞ with $S_{\mathrm{semi}\infty}$:

$$S_{\mathrm{semi}\infty} = \frac{1}{2} - \frac{j}{2} \cot\left(\tfrac{-j2\pi|m|d_z}{d}\right) + \frac{j}{2} e^{j2\pi m \frac{s}{d}} \csc\left(\tfrac{-j2\pi|m|d_z}{d}\right). \quad (16)$$

Full-wave HFSS simulations are made to validate the analytical solutions, and the comparison is shown in Fig. 8. A fair agreement can be seen for the cases shown. Figures 8(a) and (b) refer to a cascade of three layers with $\sigma = 1000$ S/m, aligned and shifted respectively. The geometrical parameters are $d = 0.095\lambda_0$, $w = 0.01\lambda_0$ and $d_z = 0.02\lambda_0$, with λ_0 being the wavelength at 300 GHz. The incident plane wave is incoming at oblique angle ($\theta = 60°, \phi = 0°$). It can be observed that the shift, while providing much higher equivalent permittivity compared to the aligned case, does not introduce a significant increase of losses. The losses for TE incidence shown in Figs. 8(a) and (b) appear to increase with the frequency at a slower rate than the TM case. This observation can be explained with the fact that the transmission coefficient

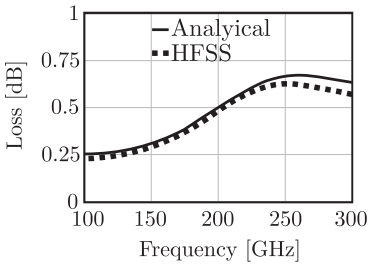

Fig. 9. Losses for TE incidence from the direction $\theta = 60°$, $\phi = 0°$ on a 5-layer aligned ADL with conductivity $\sigma = 10^6$ S/m. The geometrical parameters are $d = 0.095\lambda_0$, $w = 0.01\lambda_0$, $d_z = 0.15\lambda_0$, with λ_0 being the wavelength at 300 GHz.

for the TE case decreases significantly as the frequency grows. The low transmission signifies that most of the incident wave is reflected at the interface between the air and the ADL, thus interacts less with the lossy metal patches.

To better clarify this aspect, Fig. 9 shows a case where the total height of the ADL becomes resonant (half of the effective wavelength) within the frequency of investigation. The ADL comprises 5 layers with conductivity $\sigma = 10^6$S/m and with the same geometrical parameters as in Fig. 8(a), except for the inter-layer spacing which is $d_z = 0.15\lambda_0$. It can be observed that the losses are maximum at around 250 GHz, which also corresponds to the maximum transmission through the slabs. This effect can be interpreted by imagining that, at the resonance frequency, the wave undergoes multiple bounces within the material which add up in phase in the transmitted wave, but resulting in higher losses.

IV. Homogenization and Effective Dissipation

The analytical equivalent circuit in Fig. 7 can be used to evaluate, with minimal computational resources, the reflection and transmission coefficients of a plane wave impinging on the ADL slab, for normal and oblique incidence. These solutions can be then used to estimate the equivalent complex permittivity and permeability tensors, using the method in [15].

For example, Fig. 10 shows the resulting effective parameters of a 4-layer ADL slab with $d_z = 15\mu$m, $d = 125\mu$m, $w = 30\mu$m, $s = d/2$ and $\sigma = 10^7$ S/m. It is evident that the effective magnetic dissipation factor is much higher than the electric one, because of the loss mechanism previously explained in Fig. 6: the magnetic loss is mainly associated with the current loops supported by the patches under TE incidence.

Although both the electric and magnetic dissipation factors in Fig. 10(b) and (d) seem relatively high (in the order of 10^{-3} and 10^{-2}, respectively), it is still to be determined how these values affect the efficiency of an antenna located in the near proximity of the ADL slab. In fact, the application of ADLs proposed in [4] consists in placing ADLs above an integrated antenna to improve the front-to-back ratio.

A. Losses in ADLs for Near Source Illumination

A geometry similar to the one presented in [4] is considered in Fig. 11 and consists of a double slot antenna with an ADL superstrate. The slots have length $l_{\text{slot}} = 0.75$mm and width

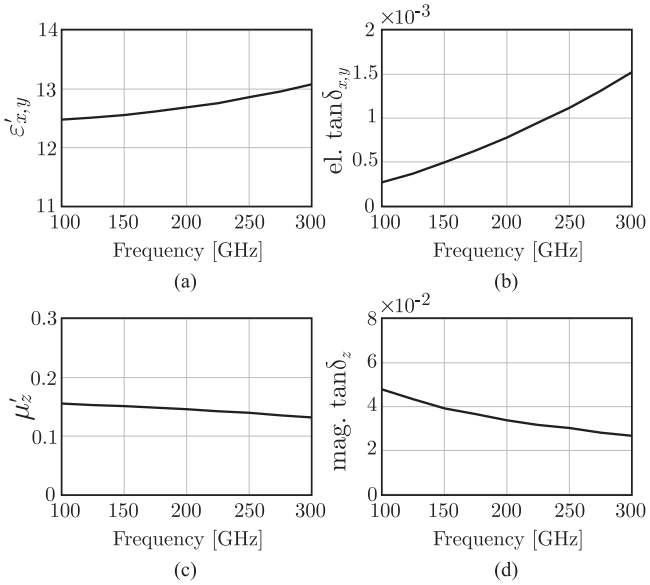

Fig. 10. Effective parameters as a function of the frequency of a 4-layer ADL with $d_z = 15\mu$m, $d = 125\mu$m, $w = 30\mu$m, $s = d/2$ and metal conductivity $\sigma = 10^7$S/m: (a) Real part of the x- and y-components of effective permittivity tensor; (b) Correspondent electric dissipation factor; (c) Real part of the z-component of effective permeability tensors; (d) Correspondent magnetic dissipation factor.

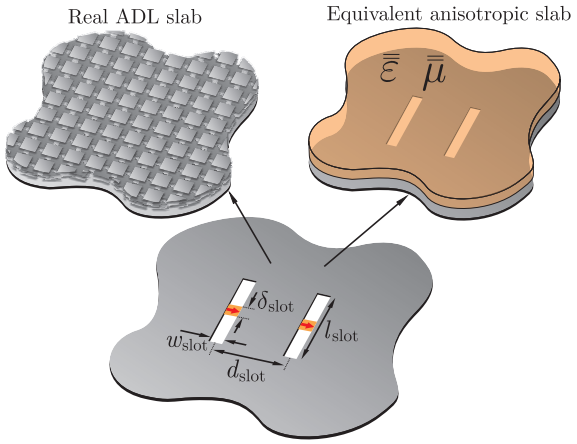

Fig. 11. Double slot antenna loaded with the ADL superstrate: (a) real ADLs and (b) homogenized equivalent material. The double slot parameters are $l_{\text{slot}} = d_{\text{slot}} = 0.75$mm, $w_{\text{slot}} = 50\mu$m, $\delta_{\text{slot}} = 0.1$mm and $h = 50\mu$m.

$w_{\text{slot}} = 50\mu$m and they are spaced by center-to-center distance $d_{\text{slot}} = 0.75$mm. The slots are excited with delta gap sources of dimensions $\delta_{\text{slot}} = 0.1$mm. A 4-layer ADL slab, with the same geometrical and electrical parameters as in Fig. 10, is placed at a distance $h = 50\mu$m above the slots. CST simulations have been performed considering two structures: the real ADL including the patches (Fig. 11(a)) and a simplified model where the ADL is replaced by an equivalent lossy anisotropic slab (Fig. 11(b)), with the homogenized effective parameters found in Fig. 10.

The simulated radiation patterns of the antenna in the presence of the ADLs are shown in Fig. 12, at 200 and 250 GHz. At these frequencies the ADL thickness becomes in

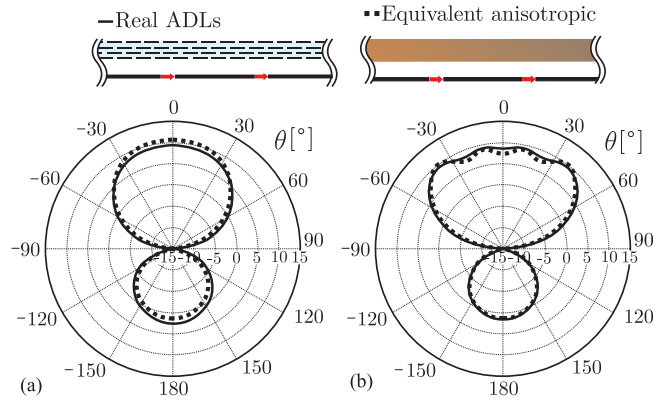

Fig. 12. Radiation patterns of the antenna with the real ADL and the equivalent homogenized slab, at (a) 200 GHz and (b) 250 GHz.

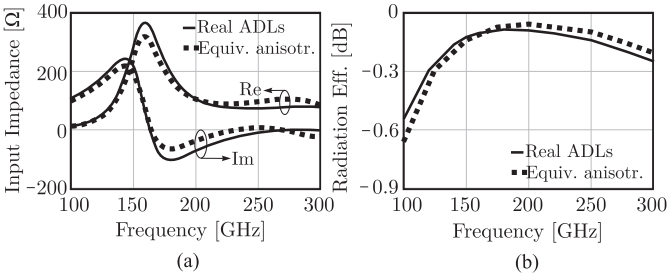

Fig. 13. (a) Input impedance and (b) radiation efficiency of the double slot with real ADL and with equivalent lossy anisotropic material.

the order a quarter of the effective wavelength, providing an enhancement of the front-to-back ratio. The simplified model with equivalent homogenized material shows similar patterns as the real ADL structure.

The active input impedance and the radiation efficiency of the antenna are also calculated and shown in Fig. 13. The comparison between the real ADL and the equivalent slab shows some differences that quantify the accuracy of the homogenization approximation. However, the approximated homogenized model can be used to give an estimation of the antenna performance, while decreasing to a great extent the computation time required for the simulation.

Finally, it can be observed that, despite the high values of the electric and magnetic $\tan\delta$ of the slab (Fig. 10(b) and (d)), the simulated radiation efficiency of the antenna in Fig. 13(b) is above 94% in the frequency range where the antenna is matched (200 to 300 GHz). This very low loss can be explained by noting that the total thickness is such that only strongly radiative leaky modes propagate within the slab, while TM surface waves are not supported and TE surface waves, responsible for high magnetic losses, are below cutoff.

V. Conclusions

Analytical formulas to describe ADLs with finite conductivity were derived. Losses are taken into account rigorously in the closed-form expressions of the equivalent layer impedance. The dependence of the dissipation losses on the polarization and direction of the incident field, as well as on the electrical thickness of the ADL slab, was highlighted.

The given formulas are functional to the design of ADLs as standalone material or in combination with antennas located in the near field. They can also be used in combination to a homogenization procedure to retrieve the effective electric and magnetic dissipation factors. Replacing the complex ADL structure with an equivalent material with homogeneous effective parameters allows to estimate the efficiency of an antenna enhanced by the ADLs with reduced computational resources. Very high radiation efficiencies (>94%) were calculated for a planar double slot antenna antennas at 250 GHz. Higher losses are expected when using ADLs for guiding waves, especially when TE modes propagate within the material.

References

[1] J. M. Edwards and G. M. Rebeiz, "High-efficiency elliptical slot antennas with quartz superstrates for silicon RFICs," *IEEE Trans. Antennas Propag.*, vol. 60, no. 11, pp. 5010-5020, Nov. 2012.

[2] D. Cavallo, W. H. Syed and A. Neto, "Artificial dielectric enabled antennas for high frequency radiation from integrated circuits," *11th Eur. Conf. Antennas Propagation*, Paris, 2017, pp. 1626-1628.

[3] D. Liu, B. Gaucher, U. Pfeiffer, and J. Grzyb, *Advanced Millimeter-Wave Technologies: Antennas, Packaging and Circuits.* Chichester, UK: John Wiley & Sons, Ltd., 2009.

[4] W. H. Syed, G. Fiorentino, D. Cavallo, M. Spirito, P. M. Sarro, and A. Neto, "Design, fabrication and measurement of 0.3 THz on-chip double-slot antenna enhanced by artificial dielectrics," *IEEE Trans. THz Sci. Tech.*, vol. 5, no. 2, pp. 288-298, Mar. 2015.

[5] E. Martini, G. M. Sardi and S. Maci, "Homogenization processes and retrieval of equivalent constitutive parameters for multisurface-metamaterials," *IEEE Trans. Antennas Propag.*, vol. 62, no. 4, pp. 2081-2092, April 2014.

[6] S. Barzegar-Parizi and B. Rejaei, "Calculation of effective parameters of high permittivity integrated artificial dielectrics," *IET Microwaves, Antennas Propag.*, vol. 9, no. 12, pp. 1287-1296, Sep. 2015.

[7] F. Mesa, R. Rodrguez-Berral, M. Garca-Vigueras, F. Medina and J. R. Mosig, "Simplified modal expansion to analyze frequency-selective surfaces: An equivalent circuit approach," *IEEE Trans. Antennas Propag.*, vol. 64, no. 3, pp. 1106-1111, March 2016.

[8] D. Cavallo, W. H. Syed, and A. Neto, "Closed-form analysis of artificial dielectric layers—Part I: Properties of a single layer under plane-wave incidence," *IEEE Trans. Antennas Propag.*, vol. 62, no. 12, pp. 6256-6264, Dec. 2014.

[9] D. Cavallo, W. H. Syed, and A. Neto, "Closed-form analysis of artificial dielectric layers—Part II: Extension to multiple layers and arbitrary illumination," *IEEE Trans. Antennas Propag.*, vol. 62, no. 12, pp. 6265-6273, Dec. 2014.

[10] D. Cavallo and C. Felita, "Analytical formulas for artificial dielectrics with nonaligned layers," *IEEE Trans. Antennas Propag.*, vol. 65, no. 10, pp. 5303-5311, Oct. 2017.

[11] G. Valerio, Z. Sipus, A. Grbic, and O. Quevedo-Teruel, "Accurate equivalent-circuit descriptions of thin glide-symmetric corrugated metasurfaces," *IEEE Trans. Antennas Propag.,* vol. 65, no. 5, pp. 2695-2700, May 2017.

[12] L. Tsai, Te-Kao Wu and J. Mayhan, "Scattering by multilayered lossy periodic strips with application to artificial dielectrics," *IEEE Trans. Antennas Propag.*, vol. 26, no. 2, pp. 257-260, Mar 1978.

[13] I. Awai, M. Furuta and T. Ishizaki, "Dissipation loss in artificial dielectrics," in *Proc. IEEE Antennas Propag. Soc. Int. Symp.*, Charleston, SC, 1-5 June 2009, pp. 1-4.

[14] M. Albani, A. Mazzinghi and A. Freni, "Rigorous MoM analysis of finite conductivity effects in RLSA antennas," *IEEE Transactions on Antennas and Propagation*, vol. 59, no. 11, pp. 4023-4032, Nov. 2011.

[15] D. Cohen and R. Shavit, "Bi-anisotropic metamaterials effective constitutive parameters extraction using oblique incidence S-parameters method," *IEEE Trans. Antennas Propag.,* vol. 63, no. 5, pp. 20712078, May 2015.